

Exploring Hilbert-Space Fragmentation on a Superconducting Processor

Yong-Yi Wang,^{1,2,||} Yun-Hao Shi^{ID, 1,2,3,||} Zheng-Hang Sun,^{4,||} Chi-Tong Chen,⁵ Zheng-An Wang,^{3,6} Kui Zhao,³ Hao-Tian Liu,^{1,2} Wei-Guo Ma^{ID, 1,2} Ziting Wang,³ Hao Li,³ Jia-Chi Zhang,^{1,2} Yu Liu,^{1,2} Cheng-Lin Deng^{ID, 1,2} Tian-Ming Li,^{1,2} Yang He,^{1,2} Zheng-He Liu,^{1,2} Zhen-Yu Peng,^{1,2} Xiaohui Song^{ID, 1,2} Guangming Xue^{ID, 3} Haifeng Yu,³ Kaixuan Huang^{ID, 3,†} Zhongcheng Xiang,^{1,2,‡} Dongning Zheng^{ID, 1,2,7,8,9} Kai Xu,^{1,2,3,7,8,9,§} and Heng Fan^{ID, 1,2,3,7,8,9,*}

¹ *Institute of Physics, Chinese Academy of Sciences, Beijing 100190, China*

² *School of Physical Sciences, University of Chinese Academy of Sciences, Beijing 100049, China*

³ *Beijing Academy of Quantum Information Sciences, Beijing 100193, China*

⁴ *Theoretical Physics III, Center for Electronic Correlations and Magnetism, Institute of Physics, University of Augsburg, Augsburg D-86135, Germany*

⁵ *Quantum Science Center of Guangdong-Hong Kong-Macao Greater Bay Area, Shenzhen, Guangdong 518045, China*

⁶ *Hefei National Laboratory, Hefei 230088, China*

⁷ *Songshan Lake Materials Laboratory, Dongguan, Guangdong 523808, China*

⁸ *CAS Center for Excellence in Topological Quantum Computation, UCAS, Beijing 100190, China*

⁹ *Mozi Laboratory, Zhengzhou 450001, China*



(Received 9 March 2024; accepted 16 January 2025; published 7 February 2025)

Isolated interacting quantum systems generally thermalize, yet there are several examples for the breakdown of ergodicity, such as many-body localization and quantum scars. Recently, ergodicity breaking has been observed in systems subjected to linear potentials, termed Stark many-body localization. This phenomenon is closely associated with Hilbert-space fragmentation, characterized by a strong dependence of dynamics on initial conditions. Here, we explore initial-state-dependent dynamics using a ladder-type superconducting processor with up to 24 qubits, which enables precise control of the qubit frequency and initial-state preparation. In systems with linear potentials, we experimentally observe distinct nonequilibrium dynamics for initial states with the same quantum numbers and energy, but with varying domain-wall numbers. Accompanied by the numerical simulation for systems with larger sizes, we reveal that this distinction becomes increasingly pronounced as the system size grows, in contrast with weakly disordered interacting systems. Our results provide convincing experimental evidence of the fragmentation in Stark systems, enriching our understanding of the weak breakdown of ergodicity.

DOI: 10.1103/PRXQuantum.6.010325

I. INTRODUCTION

In the past decades, the development of artificial quantum systems has motivated considerable studies of quantum statistical mechanics and nonequilibrium dynamics in

many-body systems [1]. As a general framework for quantum thermalization, the eigenstate thermalization hypothesis (ETH) proposes that generic closed interacting systems thermalize under their own dynamics [2–4], while the breakdown of ergodicity can typically occur in interacting systems with strong disorder, known as many-body localization (MBL) [5–7]. Recent advances reveal intermediate behavior between the two extreme limits, referred to as weak ergodicity breaking, including phenomena such as quantum many-body scars [8–12] and Hilbert-space fragmentation (HSF) [13–19]. In weak ergodicity breaking systems, a small fraction of nonthermal eigenstates coexist within the majority of the thermal spectrum, allowing for halted thermalization under certain initial conditions [20].

As a prominent example of weak ergodicity breaking, HSF has been extensively explored theoretically in

*Contact author: hfan@iphy.ac.cn

†Contact author: huangkx@baqis.ac.cn

‡Contact author: zcxiang@iphy.ac.cn

§Contact author: kaixu@iphy.ac.cn

||These authors contributed equally to this work.

dipole-moment conserving systems, where the Hilbert space fragments into exponentially many disconnected Krylov subspaces due to the interplay between charge and dipole conservation, leading to the strong dependence of the dynamics on the initial conditions [13–15,21]. On the other hand, systems subjected to a linear potential (hereinafter referred to as Stark systems) can also exhibit MBL-like behavior, such as long-lived initial state memory and multifractality, termed Stark many-body localization (SMBL) [22–27]. Experimental studies of SMBL have been conducted using various experimental platforms [28–32]. In these systems subjected to a linear potential, the emergence of dipole moment has raised questions and debates about its relationship with HSF [14,24,33–35]. A previous work showed a significant dependence of the dynamics on the initial doublon fraction in the tilted one-dimensional Fermi-Hubbard model, but the initial conditions considered do not possess the same quantum numbers and energy [32]. Actually, the dynamics is profoundly related to the energy of the chosen initial states even in disordered interacting systems, as a consequence of many-body mobility edge [36,37]. Therefore, a direct demonstration of HSF in Stark systems requires a more thorough investigation into the dynamics for the initial states with the same quantum numbers and energy, excluding the potential influences stemming from different total charge and emergent dipole moment, as well as many-body mobility edges.

In this work, leveraging the precise control and flexibility of our ladder-type superconducting processor, we engineer the Hamiltonian and prepare various initial states with the same quantum numbers (charge and dipole moment) and energy for systems with up to 24 qubits. Applying site-dependent frequency deviations to individual qubits precisely, we observe distinct dynamical behavior in the Stark systems for initial states featuring varying domain-wall numbers, even at a very small gradient.

Moreover, recent work [38] suggests a dependence of the dynamics on the domain-wall number in the initial states in disordered systems. To distinguish this phenomenon in disordered systems from HSF, we also investigate the dependence on the domain-wall number in weakly disordered systems, specifically in the ergodic phase. We demonstrate that, in weakly disordered systems, slow relaxation for initial states with small domain-wall numbers is a finite-time effect. In contrast, in systems with a weak linear potential, the distinct dynamics associated with different domain-wall numbers, persisting over long timescales, become increasingly pronounced as the system size grows.

In addition, the efficient single-shot simultaneous readout enables us to experimentally measure the dynamics of participation entropy (PE), which directly characterizes the available Hilbert space for a certain initial state [37,39,40]. The limited growth of PE observed in systems subjected

to a linear potential reveals that an initial state with a small domain-wall number can only spread within a limited fraction of the Hilbert space, providing direct evidence of HSF in Stark systems. For larger systems, where measuring the PE of the entire system becomes challenging, we propose a practical scheme to estimate the upper bound of PE by experimentally measuring subsystems of moderate length, from which we can also extract key evidence of HSF.

II. MODEL AND SETUP

Our experiments utilize a quantum processor equipped with a two-legged ladder structure consisting of 30 transmon qubits, as shown in Fig. 1(a). The effective Hamiltonian of the qubit-ladder processor reads [41–43]

$$\begin{aligned} \frac{\hat{H}}{\hbar} = & \sum_{\langle jm; j'm' \rangle} J_{jm; j'm'} \left(\hat{\sigma}_{jm}^+ \hat{\sigma}_{j'm'}^- + \hat{\sigma}_{jm}^- \hat{\sigma}_{j'm'}^+ \right) \\ & + \sum_{m=1,2} \sum_{j=1}^L W_{jm} \hat{\sigma}_{jm}^+ \hat{\sigma}_{jm}^-, \end{aligned} \quad (1)$$

where $\hbar = h/2\pi$ denotes the Planck constant, L is the length of the ladder, $\hat{\sigma}_{jm}^+ (\hat{\sigma}_{jm}^-)$ is the two-level raising (lowering) operator for the qubit Q_{jm} . Here, the first summation runs over all nearest- and next-nearest-neighboring sites (j, m) and (j', m') with the averaged nearest-neighboring qubit-qubit coupling $\bar{J}_{NN}/2\pi \simeq 7$ MHz and next-nearest-neighboring $\bar{J}_{NNN} \lesssim \bar{J}_{NN}/6$ (see the Supplemental Material [44] for coupling strengths in details). The on-site potential, denoted as W_{jm} , can be adjusted by applying fast flux bias to the Z control lines of qubits. This flexibility enables the tuning of W_{jm} to both Stark (linear) potentials $W_{jm}/\bar{J}_{NN} = -j\gamma$, as well as random potentials W_{jm}/\bar{J}_{NN} drawn from a uniform distribution in $[-W, W]$, facilitating the quantum simulation of both SMBL and conventional MBL.

Utilizing a generalized form of Jordan-Wigner transformation [45,46], the approximating ladder-XX model can be mapped to an interacting spinless fermion model. As the gradient γ (or the disorder strength W) increases, a transition from ergodicity to MBL exists in this typical nonintegrable model [44]. One can expect that in the regime of a large gradient γ , the conservation of total $U(1)$ charge $\hat{Q} \equiv \sum_{j,m} \hat{\sigma}_{jm}^+ \hat{\sigma}_{jm}^-$, together with the emergent conservation of dipole moment $\hat{P} \equiv \sum_{j,m} j \hat{\sigma}_{jm}^+ \hat{\sigma}_{jm}^-$, gives rise to HSF, so that the system would exhibit distinct dynamics with different initial states $|\psi_0\rangle$.

For $|\psi_0\rangle$ considered in this work, the initial spin distribution is identical in the two rows of the ladder. These initial states share the same $Q = \langle \hat{Q} \rangle$, $P = \langle \hat{P} \rangle$, and energy $E = \langle \psi_0 | \hat{H} | \psi_0 \rangle$, but vary in terms of total domain-wall number, defined as $n_{DW} = \sum_{j=1}^{L-1} (1 - \langle \hat{\sigma}_j^z \hat{\sigma}_{j+1}^z \rangle)/2$, with $\hat{\sigma}_j^z = (\hat{\sigma}_{j,1}^z + \hat{\sigma}_{j,2}^z)/2$. Specifically, we examine two initial states

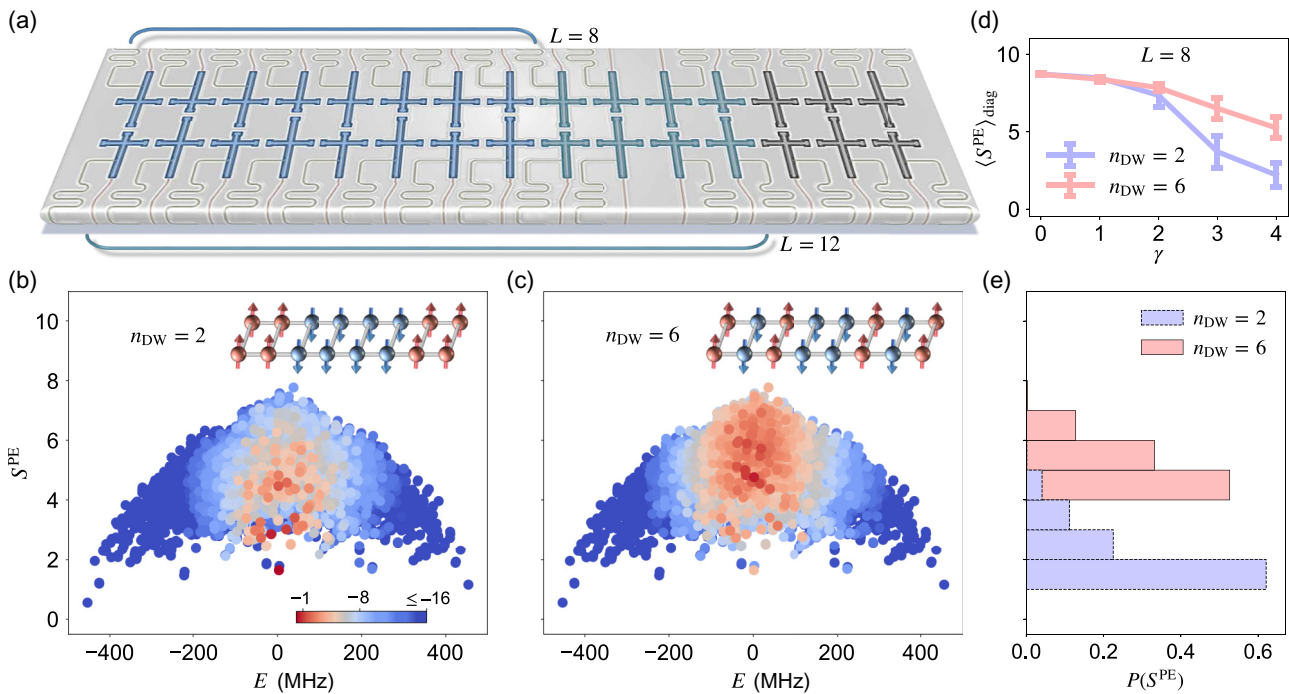


FIG. 1. Experimental setup. (a) Schematic representation of the ladder-type superconducting processor. For the experiment, $L(8 \& 12) \times 2$ qubits of the 30-qubit ladder are utilized, with nearest-neighboring $\tilde{J}_{\text{NN}}/2\pi \simeq 7$ MHz and next-nearest-neighboring couplings $\tilde{J}_{\text{NNN}} \lesssim \tilde{J}_{\text{NN}}/6$. (b),(c) Participation entropy of eigenstates for Hamiltonian [Eq. (1)] with $\gamma = 4$, colored by the logarithm of the eigenstate occupation numbers $\log_{10} |\langle \psi_0 | E_n \rangle|^2$ for the initial state (b) $|\psi_{n_{\text{DW}}=2}\rangle = |11000011\rangle$, and (c) $|\psi_{n_{\text{DW}}=6}\rangle = |10100101\rangle$, with $|0(1)\rangle$ denotes the ground (excited) state $|0(1)\rangle$ on both legs of each ladder rung. (d) Diagonal ensemble average of the PE for different gradients γ , with the errorbar presenting the standard deviation. (e) Histogram of the participation entropy with $\gamma = 4$ in the diagonal ensembles corresponding to the initial states $|\psi_{n_{\text{DW}}=2}\rangle$ and $|\psi_{n_{\text{DW}}=6}\rangle$.

for the system length $L = 8$: $|\psi_{n_{\text{DW}}=2}\rangle = |11000011\rangle$ and $|\psi_{n_{\text{DW}}=6}\rangle = |10100101\rangle$, where $|0(1)\rangle$ denotes the ground (excited) state of the single qubit $|0(1)\rangle$ on both legs of each ladder rung [see the insets in Figs. 1(b) and 1(c)].

To quantify the localization in Hilbert space of spin configurations, we can calculate the PE of all eigenstates with exact diagonalization [37,39,40], defined as $S^{\text{PE}}(n) = -\sum_i^{\mathcal{N}} p_i(n) \log p_i(n)$, where \mathcal{N} is the dimension of Hilbert space, and $p_i(n) = |\langle i | E_n \rangle|^2$ with $\{|i\rangle\}$ being the spin configuration basis (i.e., $\{\sigma^z\}$). Thus, $S^{\text{PE}} = 0$ if the state is a single configuration, and $S^{\text{PE}}_{\text{GOE}} = \log 0.482\mathcal{N}$ for Gaussian random states [44,47]. In Figs. 1(b) and 1(c), the PE of eigenstates is displayed for the Hamiltonian [Eq. (1)] with a Stark potential at $\gamma = 4$. The colorbars represent the eigenstate occupation numbers $|C_n|^2 \equiv |\langle \psi_0 | E_n \rangle|^2$, indicating the weight of eigenstate $|E_n\rangle$ in the diagonal ensemble [2,3], with respect to $|\psi_0\rangle = |\psi_{n_{\text{DW}}=2}\rangle$ and $|\psi_{n_{\text{DW}}=6}\rangle$, respectively. Different from the ETH prediction, substantial fluctuations in PE are observed across the eigenstates within a narrow window around $E = 0$.

Notably, as depicted in Fig. 1(e), $|\psi_{n_{\text{DW}}=2}\rangle$ tends to predominantly overlap with a small number of eigenstates with relatively low PE, whereas the weight distribution

for $|\psi_{n_{\text{DW}}=6}\rangle$ spreads over a greater number of eigenstates with higher PE. We calculate the diagonal ensemble average of the PE $\langle S^{\text{PE}} \rangle_{\text{diag}} \equiv \sum_n |C_n|^2 S^{\text{PE}}(n)$, and the variance $\sigma^2 \equiv \sum_n |C_n|^2 [S^{\text{PE}}(n) - \langle S^{\text{PE}} \rangle_{\text{diag}}]^2$, to characterize these two distributions for various γ . We observe that as γ increases, the averages between the two distributions of the PE increasingly diverge, with the standard deviation being smaller than the difference between their averages [see Fig. 1(d)], suggesting a decrease in the overlap of the distributions. At $\gamma = 4$, the diagonal-ensemble predictions of PE is $\langle S^{\text{PE}} \rangle_{\text{diag}} = 5.24 \pm 0.68$ and 2.20 ± 0.79 corresponding to $|\psi_0\rangle = |\psi_{n_{\text{DW}}=6}\rangle$ and $|\psi_{n_{\text{DW}}=2}\rangle$, respectively. This indicates that these two states, respectively, reside within nearly disconnected fragments, with $|\psi_{n_{\text{DW}}=2}\rangle$ more localized within a smaller fragment in the Hilbert space than $|\psi_{n_{\text{DW}}=6}\rangle$. The results for different γ , similar behavior in entanglement entropy, and the relation between the PE and domain-wall numbers can be found within the Supplemental Material [44].

III. INITIAL-STATE-DEPENDENT DYNAMICS

In contrast to ergodic dynamics, where memory of the initial conditions is hidden in global operators, in MBL

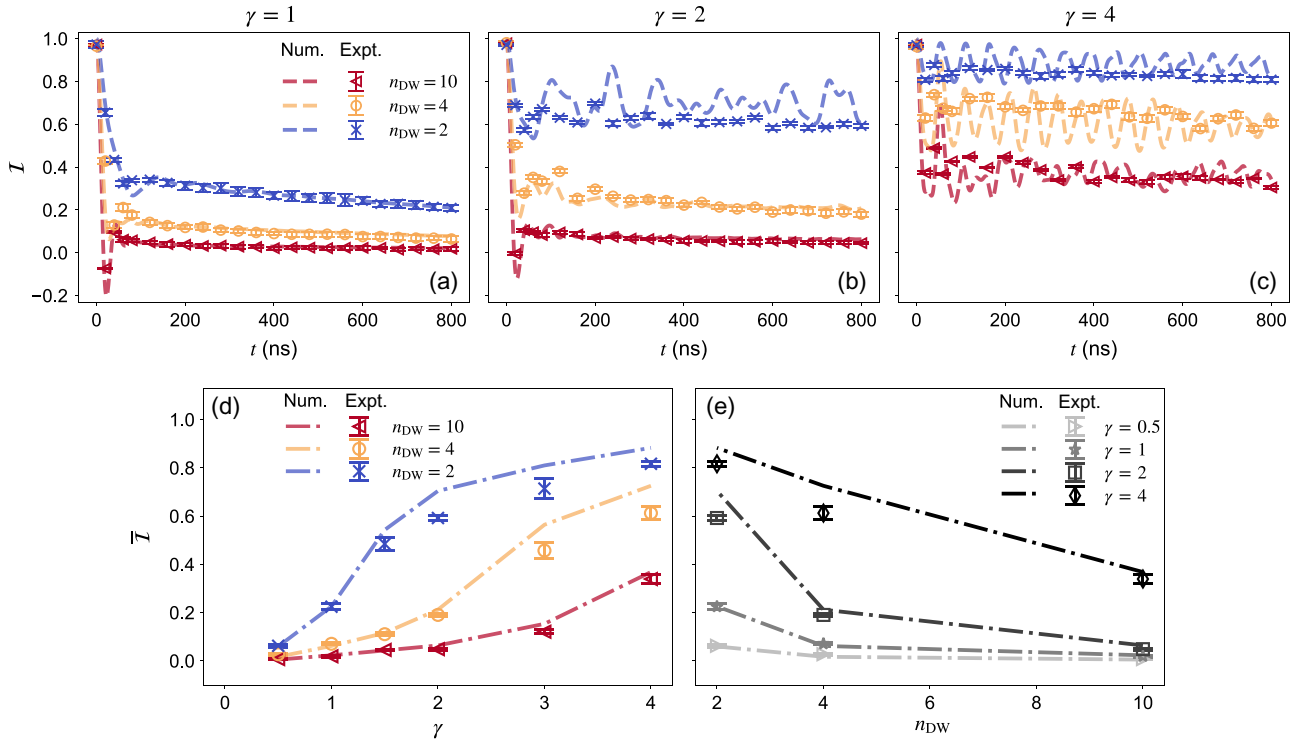


FIG. 2. Initial-state-dependent dynamics of imbalance in the 12×2 ladder. (a)–(c) The time evolution of the imbalance $\mathcal{I}(t)$ for different initial states $|\psi_{n_{DW}=2}\rangle = |1\ 1\ 1\ 0\ 0\ 0\ 0\ 0\ 0\ 1\ 1\rangle$, $|\psi_{n_{DW}=4}\rangle = |1\ 1\ 0\ 0\ 0\ 1\ 1\ 0\ 0\ 0\ 1\rangle$, and $|\psi_{n_{DW}=10}\rangle = |1\ 0\ 1\ 0\ 1\ 0\ 0\ 1\ 0\ 1\ 0\rangle$ at gradients $\gamma = 1, 2$, and 4 , respectively. Points are experimental data, each averaged over 5000 repetitions, and the dashed lines are numerical simulation. (d) The late-time averaged imbalance $\bar{\mathcal{I}}$ as a function of the gradient γ for initial states with different domain-wall numbers n_{DW} . (e) The late-time averaged imbalance $\bar{\mathcal{I}}$ as a function of n_{DW} for different γ . Averages are taken over a time window from 600 to 800 ns. Error bars represent the standard deviation.

systems, memory of the initial conditions can be preserved in local observables for generic high-energy initial states at long times after sudden quench [5–7]. To quantify the preservation of the information encoded in the initial state, we consider the imbalance generalized for any initial product state in the $\{\sigma^z\}$ [30,36,48], defined as

$$\mathcal{I} = \frac{1}{2L} \sum_{jm} \langle \psi_0 | \hat{\sigma}_{jm}^z(t) \hat{\sigma}_{jm}^z(0) | \psi_0 \rangle. \quad (2)$$

The generalized imbalance will relax from initial value $\mathcal{I} = 1$ to 0 if the system thermalizes, while it will maintain a finite value at long times if the system fails to thermalize.

To observe the initial-state-dependent dynamics due to HSF, we consider three typical initial states for the system length $L = 12$, including $|\psi_{n_{DW}=2}\rangle = |1\ 1\ 1\ 0\ 0\ 0\ 0\ 0\ 0\ 1\ 1\rangle$, $|\psi_{n_{DW}=4}\rangle = |1\ 1\ 0\ 0\ 0\ 1\ 1\ 0\ 0\ 0\ 1\rangle$, and $|\psi_{n_{DW}=10}\rangle = |1\ 0\ 1\ 0\ 1\ 0\ 0\ 1\ 0\ 1\ 0\rangle$. We prepare these initial states with the same quantum numbers and energy but different domain-wall numbers, by simultaneously applying π pulses to half of the qubits. Calibrating the rectangular Z pulses for all qubits to create Stark potentials, we measure the generalized imbalance \mathcal{I} for different initial states following evolution over time t . The experimental data at $\gamma = 1, 2$, and 4

are depicted in Figs. 2(a)–2(c), along with numerical simulation [44]. We note that for $\gamma = 1, 2$, the average ratio of adjacent level spacings $\langle r \rangle \gtrsim 0.5$, close to the prediction of the Gaussian orthogonal ensemble, while $\langle r \rangle \lesssim 0.4$ for $\gamma = 4$, exhibiting Poisson statistics [37,44,49,50]. Therefore, at $\gamma = 4$, the imbalance oscillates around a finite value after a fast drop at short times for all three states, signifying a complete breakdown of ergodicity. At both $\gamma = 1$ and 2, the imbalance for $|\psi_0\rangle = |\psi_{n_{DW}=10}\rangle$ relaxes to zero, in accordance with ergodic dynamics. However, the relaxation gradually slows down as n_{DW} decreases. For $\gamma = 2$, the imbalance for $|\psi_0\rangle = |\psi_{n_{DW}=2}\rangle$ has already exhibited pronounced oscillations around a value significantly above zero with negligible decay.

We then average the late-time imbalance over a time window from 600 to 800 ns, which is plotted against γ and n_{DW} in Figs. 2(d) and 2(e), respectively. On the one hand, the late-time imbalance for all initial states exhibits a clear upward trend as γ increases. On the other hand, we observe a monotonic decrease in the late-time imbalance as n_{DW} decreases. For initial states with smaller n_{DW} , the late-time imbalance displays a quicker rise as γ increases. By selecting initial states with identical quantum numbers and energy, the above experimental results demonstrate the

initial-state-dependent dynamics concerning domain-wall numbers in Stark systems, which is a significant feature of HSF and weak breakdown of ergodicity.

IV. COMPARISON WITH WEAKLY DISORDERED SYSTEMS

According to the ETH, a fully delocalized regime exists in the disordered interacting systems with weak disorder, where the choice of the initial state is of no significance at long times [38,51]. However, in terms of the ETH in its strong sense, numerical evidence has been put forward for the absence of an ETH-MBL transition in Stark systems due to HSF [33]. The question of whether HSF will lead to distinctions between Stark systems and disordered systems is a crucial aspect to explore. Here, we focus on the Hamiltonian [Eq. (1)] with the gradient $\gamma = 1$, and the disorder strengths $W = 3$. For these parameters, $\langle r \rangle$ remains close to 0.531, often viewed as a signature of ergodicity [44]. In other words, we focus on systems with weak Stark and disordered potentials, which exhibit ETH-like level statistics.

For both models, we measure the generalized imbalance for $|\psi_0\rangle = |\psi_{n_{\text{DW}}=2}\rangle$ and $|\psi_{n_{\text{DW}}=L-2}\rangle$ with system lengths $L = 8$ and 12. The experimental data and numerical results are presented in Fig. 3. We can see that the imbalance for $|\psi_0\rangle = |\psi_{n_{\text{DW}}=L-2}\rangle$ relaxes to zero in a short time for both Stark systems and disordered systems, irrespective of system size.

However, in Stark systems, an evident slowdown in relaxation can be observed for $|\psi_0\rangle = |\psi_{n_{\text{DW}}=2}\rangle$, which becomes more evident with increasing system size [see Figs. 3(a) and 3(b)]. A significantly higher late-time imbalance for $L = 12$ compared to $L = 8$ suggests a nonvanishing imbalance for systems with a sufficiently large size. This phenomenon persists even for a smaller gradient $\gamma = 0.5$ [44].

In contrast, in weakly disordered systems, we can merely observe a slightly slower thermalization for $|\psi_0\rangle = |\psi_{n_{\text{DW}}=2}\rangle$ compared to $|\psi_{n_{\text{DW}}=L-2}\rangle$, with the disorder-average imbalance approaching zero at long times for both initial states. This behavior holds true for both system lengths $L = 8$ and 12, as shown in Figs. 3(c) and 3(d), which starkly contrasts with the observation in Stark systems. A more quantitative analysis of the imbalance decay in the two models is provided within the Supplemental Material [44].

To elucidate the finite-size effect in the two systems [52,53], within the Supplemental Material [44], we present numerical simulations of the dynamics with lengths up to $L = 20$ using matrix-product-state (MPS) techniques. Moreover, we consider a longer evolution time up to $t = 40 \mu\text{s}$ ($J_{\text{NN}}t \sim 2 \times 10^3$) to provide a definitive observation of the initial-state-dependent dynamics in Stark systems. We show that, in weakly disordered systems, although the

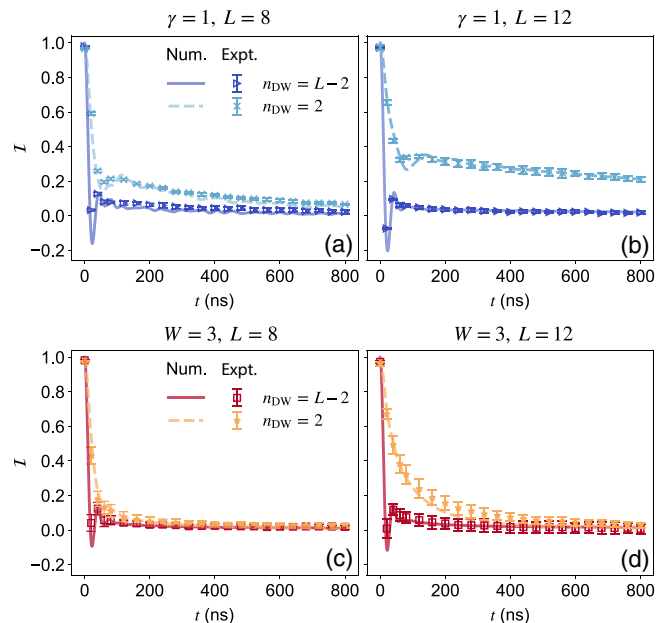


FIG. 3. Time evolution of imbalance for initial states $|\psi_0\rangle = |\psi_{n_{\text{DW}}=2}\rangle$ and $|\psi_{n_{\text{DW}}=L-2}\rangle$ in different systems: (a) Stark system with the gradient $\gamma = 1$ for $L = 8$, and (b) Stark system with $\gamma = 1$ for $L = 12$; (c) disordered system with the disorder strength $W = 3$ for $L = 8$, and (d) disordered system with $W = 3$ for $L = 12$. In Stark systems (a),(b), points are experimental data, each averaged over 5000 repetitions with error bars indicating the standard deviation. In disordered systems (c),(d), the experimental data points are the average of 20 disorder realizations with 5000 repetitions for each realization, and the error bar shows the standard error of the mean. Lines represent numerical simulation.

dynamics for the two-domain-wall initial state suffers from a strong finite-time effect, the imbalance is expected to approach zero eventually in the thermodynamic limit. This behavior is consistent with “strong” ETH, where the long-time behavior of local observables does not depend on the initial states, provided they share the energy and quantum numbers. In contrast, the Stark system with a small linear potential exhibits a robust dynamical signature of “weak” ETH, where a small set of eigenstates may violate ETH, leading to the initial-state-dependent dynamics.

V. DYNAMICAL SIGNATURE OF HSF VIA PARTICIPATION ENTROPY

As discussed above, the Hilbert space tends to fragment into many disconnected Krylov subspaces with different dimensions in Stark systems. A direct quantity reflecting the extent to which a time-evolved state $|\psi(t)\rangle$ spreads over the Hilbert space [36,54] is the dynamical PE, defined as

$$S^{\text{PE}}(t) = - \sum_i^N p_i(t) \log p_i(t), \quad (3)$$

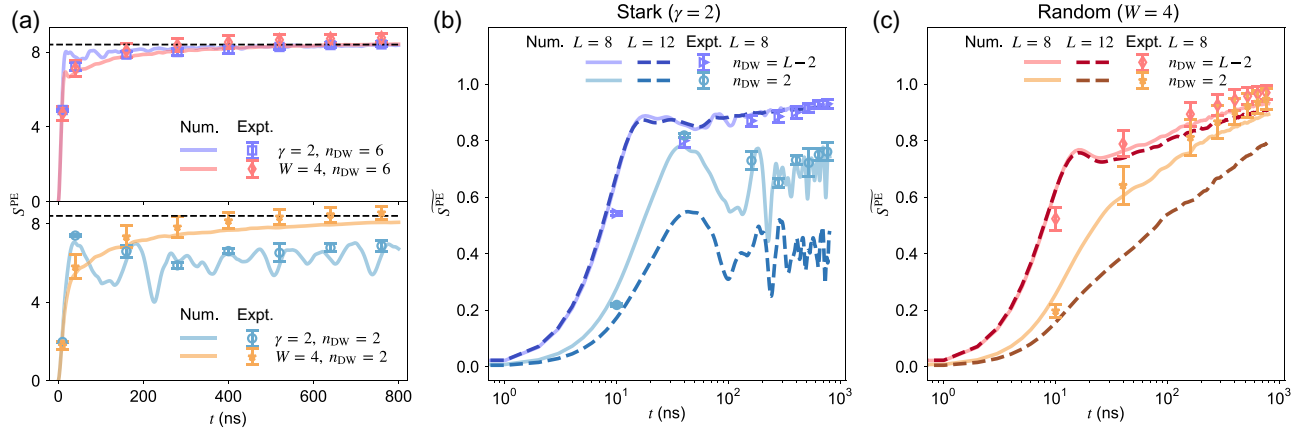


FIG. 4. Time evolution of participation entropy. (a) Dynamical participation entropy in the Stark system with $\gamma = 2$ and the disordered system with $W = 4$ for different initial states $|\psi_0\rangle = |\psi_{n_{\text{DW}}=6}\rangle$ (upper panel) and $|\psi_{n_{\text{DW}}=2}\rangle$ (lower panel) with the system length $L = 8$. For $|\psi_0\rangle = |\psi_{n_{\text{DW}}=6}\rangle$, the numerical results of the late-time S^{PE} is around 8.4 in both systems, marked by the horizontal dashed lines in both panels. (b),(c) Normalized PE $\widetilde{S}^{\text{PE}} = S^{\text{PE}}/S_T^{\text{PE}}$ with the same experimental data as (a) against the logarithm of time, in (b) the Stark system with $\gamma = 2$ and (c) the disordered system with $W = 4$. Numerical results are depicted by lines for $L = 8$ and 12. The experimental data for S^{PE} in Stark systems are obtained from five sets of independent experiments, each consisting of 5×10^5 repeated single-shot measurements. For disordered systems, data are from 20 disorder realizations, each with 5×10^5 measurements. Error bars indicate the standard deviation.

with the multiqubit probabilities $p_i(t) = |\langle\psi(t)|i\rangle|^2$. For ergodic dynamics, the dynamical PE increases from $S^{\text{PE}}(0) = 0$ for any initial product state to the late-time value $S_T^{\text{PE}} = \log \mathcal{N} - 1 + \gamma_e$ (with γ_e Euler's constant) [44,55]. The dynamical PE determined by the multiqubit probabilities can be observed with our superconducting processor thanks to its efficient multiqubit simultaneous readout capability. Applying a Stark potential with $\gamma = 2$ and a random potential with $W = 4$ to the system, we track the time evolution of the multiqubit probabilities with site-resolved simultaneous readout at different times t . For the calculation of the PE, the experimental data of the multiqubit probabilities in Fig. 4 are obtained from 5×10^5 repeated measurements and postselected within the $Q = L$ sector. As shown in Fig. 4(a), the initial product states, as Fock states, gradually propagate and cover the available Hilbert space at long times, reflected by the increase of PE. For both models, dynamics for $|\psi_0\rangle = |n_{\text{DW}} = 6\rangle$ approaches similar values of PE at long times. However, in a random potential, the PE for $|\psi_0\rangle = |\psi_{n_{\text{DW}}=2}\rangle$ increases and eventually approaches the late-time value for $|\psi_{n_{\text{DW}}=6}\rangle$ [marked by dashed lines in Fig. 4(a)], while in a Stark potential, it oscillates at a lower value, suggesting that $|\psi_{n_{\text{DW}}=2}\rangle$ can only propagate in a restricted fraction of the Hilbert space.

In Figs. 4(b) and 4(c), we plot the experimental data of normalized PE $\widetilde{S}^{\text{PE}} = S^{\text{PE}}/S_T^{\text{PE}}$ against the logarithm of time, with numerical results for $L = 12$, in systems with small Stark and random potentials, respectively. In Stark systems, we observe that the data of normalized PE for $|\psi_{n_{\text{DW}}=L-2}\rangle$ nearly coincide for different system sizes,

while those for $|\psi_{n_{\text{DW}}=2}\rangle$ decreases with the increasing system size. This indicates that $|\psi_{n_{\text{DW}}=L-2}\rangle$ can spread in a fraction of Hilbert space whose dimension scales with the size of the entire Hilbert space, while the dimension of Krylov subspace corresponding to $|\psi_{n_{\text{DW}}=2}\rangle$ becomes vanishingly small in the thermodynamic limit [44]. In contrast, in disordered systems, $\widetilde{S}^{\text{PE}}$ exhibits unceasing growth within the experimental time for both initial states (and approaches a similar value of $\widetilde{S}^{\text{PE}} \sim 1$ over a longer time [44]), despite differences in relaxation. The comparison to disordered interacting systems further reveals a distinctive characteristic in Stark systems, where the initial-state-dependent dynamics is closely associated with disconnected Krylov subspaces with different scaling behaviors.

For a system with the length of 12 or larger, it is a challenging experimental task to measure PE directly for the entire system. To address this challenge, we introduce the concept of local PE. Let us first divide the system into two parts: the subsystem \mathcal{S} and its complement. As depicted in the upper part of Fig. 5, the subsystem \mathcal{S} includes consecutive $l \times 2$ qubits $\mathcal{S}(j; l) = \{Q_{j,m}, Q_{j+1,m}, \dots, Q_{j+l-1,m}\}$ with $m = 1, 2$. The local PE can then be defined as the PE for the subsystem \mathcal{S} , which is given by

$$S^{\text{PE}}[\mathcal{S}] = \sum_i p_i^{\mathcal{S}} \log p_i^{\mathcal{S}}, \quad (4)$$

where $p_i^{\mathcal{S}}$ denotes the probabilities of a time-evolved state in spin configuration basis $|i\rangle^{\mathcal{S}} \in \{|i_Q\rangle | i_Q \in \{0, 1\}, Q \in \mathcal{S}\}$ for the subsystem $\mathcal{S}(j; l)$. When $l = L$, the local PE corresponds to the PE of the entire system. Regardless of

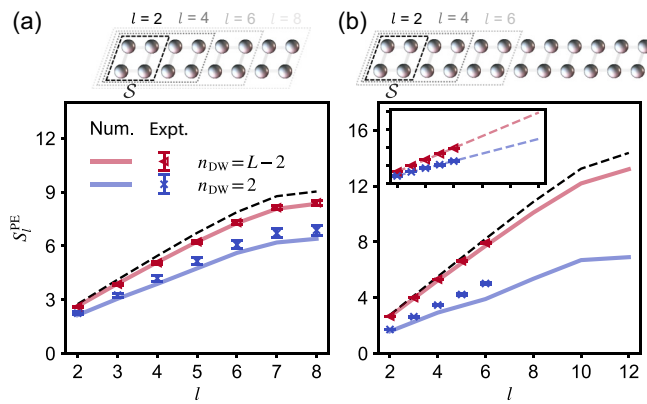


FIG. 5. Late-time local participation entropy of subsystems. (a) The late-time local participation entropy in the Stark system with $\gamma = 2$ for $L = 8$. Lines denote numerical simulations, while points are experimental data averaged over five sets of independent experiments, each set consisting of 5×10^5 repeated single-shot measurements. The error bars denote the standard deviation. (b) Same as (a), but for $L = 12$, with each set consisting of 1×10^6 repeated single-shot measurements. The data points are measured around $t \approx 800$ ns. The black dashed lines denote local participation entropies of random pure states for (a) $L = 8$ and (b) $L = 12$, respectively. Inset in (b), the dashed lines, colored according to the different initial states, denote the fit of the data from $l = 2$ to $l = 6$ with a linear function. The fitted functions are $f(l) = 1.31l + 0.05$ for $|\psi_0\rangle = |\psi_{n_{\text{DW}}=L-2}\rangle$, and $f(l) = 0.82l + 0.14$ for $|\psi_0\rangle = |\psi_{n_{\text{DW}}=2}\rangle$, respectively.

the system length L , local PE can be efficiently measured in quantum processors with relatively small number of measurements for subsystems of moderate length l [44].

In Fig. 5, we present both the numerical and experimental results of the late-time spatially averaged local PE $S_l^{\text{PE}} = \langle S^{\text{PE}}[\mathcal{S}(j; l)]_j \rangle$ ($\langle \dots \rangle_j$ denotes the average over all possible subsystems with consecutive $l \times 2$ qubits) for the Stark system with $\gamma = 2$, around $t \approx 800$ ns, for system lengths $L = 8$ [Fig. 5(a)] and $L = 12$ [Fig. 5(b)]. For these two system lengths L , we observe that the local PE increases approximately linearly with the subsystem length l for both initial states $|\psi_0\rangle = |\psi_{n_{\text{DW}}=2}\rangle$ and $|\psi_{n_{\text{DW}}=L-2}\rangle$, except for a downward bending as l approaches the entire system length L . This downward bending is also observed for random pure states, i.e., the late-time states for fully ergodic systems (see the black dashed lines in Fig. 5). We argue that this downward bending is a result of the conservation of total $U(1)$ charge, and becomes more moderate with larger system sizes [44]. This behavior suggests a practical and scalable approach for estimating the upper bound of PE by fitting the local PE measured in subsystems of moderate length l , and then extrapolating to $l = L$.

For $L = 12$, as shown in the inset of Fig. 5(b), we fit the experimental data for $l = 2$ to $l = 6$ with a linear function, and extrapolate to estimate the upper bound for the PE of the entire system, denoted as $S_{\text{est}}^{\text{PE}}$. The difference

in estimated PE $\Delta S_{\text{est}}^{\text{PE}} \approx 6$ between the two initial states reflects the significant discrepancy between the Krylov subspaces corresponding to the two initial states.

VI. CONCLUSIONS AND OUTLOOK

In summary, we have reported the experimental observation of distinctively initial-state-dependent dynamics in Stark systems, by studying the dynamics of imbalance and PE for initial states with varying domain-wall numbers. Our experimental results are primarily relevant for system sizes up to 12×2 and timescales of tunneling times up to $\bar{T}_{\text{NN}} \sim 40$, qualitatively showcasing signatures of HSF in Stark systems. This experiment elucidates the crucial distinctions between the systems with weak linear and disordered potentials, demonstrating weak ETH due to HSF in the former and strong ETH in the latter. The distinctions are further numerically demonstrated for larger systems and longer timescales using MPS techniques within the Supplemental Material [44]. Moreover, the close relation between the late-time imbalance and domain-wall numbers of initial states indicates the presence of a more intricate landscape of the mobility edge in weak ergodicity-breaking systems like Stark systems [56,57], in contrast with disorder-driven MBL where the mobility edge relies solely on energy [36].

The efficient readout of our superconducting processor enables the measurement of PE, offering direct evidence of HSF. However, it is a challenging experimental task for systems with a length of 12 or larger. To this end, we propose a scheme for estimating the upper bound of PE by measuring the local PE, which requires relatively fewer experimental measurements. As a direct measure of the Krylov subspace dimension, the PE, along with the associated local PE, merits systematic study in typical toy models of HSF, such as pair-hopping models [13,14,18,21]. This approach will also enable further investigations of HSF in Stark systems or other higher-dimensional weak ergodicity-breaking systems [58,59].

ACKNOWLEDGMENTS

This work was supported by the National Natural Science Foundation of China (Grants No. 92265207, No. T2121001, No. 92365301, No. T2322030, No. 12122504, No. 12274142, No. 12475017, and No. 12204528), the Innovation Program for Quantum Science and Technology (Grant No. 2021ZD0301800), the Beijing Nova Program (Grant No. 20220484121), the Natural Science Foundation of Guangdong Province (Grant No. 2024A1515010398), Scientific Instrument Developing Project of Chinese Academy of Sciences (Grant No. YJKYYQ20200041), the Key-Area Research and Development Program of Guang-Dong Province (Grants No. 2018B030326001

and No. 2020B0303030001), the State Key Development Program for Basic Research of China (Grant No. 2017YFA0304300), the China Postdoctoral Science Foundation (Grant No. GZB20240815), and the support from the Synergetic Extreme Condition User Facility (SECUF) in Huairou District, Beijing. Devices were made at the Nanofabrication Facilities at Institute of Physics, CAS in Beijing.

DATA AVAILABILITY

The data that support the findings of this article are not publicly available upon publication because it is not technically feasible and/or the cost of preparing, depositing, and hosting the data would be prohibitive within the terms of this research project. The data are available from the authors upon reasonable request.

-
- [1] I. M. Georgescu, S. Ashhab, and F. Nori, Quantum simulation, *Rev. Mod. Phys.* **86**, 153 (2014).
 - [2] M. Rigol, V. Dunjko, and M. Olshanii, Thermalization and its mechanism for generic isolated quantum systems, *Nature* **452**, 854 (2008).
 - [3] L. D'Alessio, Y. Kafri, A. Polkovnikov, and M. Rigol, From quantum chaos and eigenstate thermalization to statistical mechanics and thermodynamics, *Adv. Phys.* **65**, 239 (2016).
 - [4] J. M. Deutsch, Eigenstate thermalization hypothesis, *Rep. Prog. Phys.* **81**, 082001 (2018).
 - [5] R. Nandkishore and D. A. Huse, Many-body localization and thermalization in quantum statistical mechanics, *Annu. Rev. Condens. Matter Phys.* **6**, 15 (2015).
 - [6] E. Altman, Many-body localization and quantum thermalization, *Nat. Phys.* **14**, 979 (2018).
 - [7] D. A. Abanin, E. Altman, I. Bloch, and M. Serbyn, Colloquium: Many-body localization, thermalization, and entanglement, *Rev. Mod. Phys.* **91**, 21001 (2019).
 - [8] H. Bernien, S. Schwartz, A. Keesling, H. Levine, A. Omran, H. Pichler, S. Choi, A. S. Zibrov, M. Endres, M. Greiner, V. Vuletic, and M. D. Lukin, Probing many-body dynamics on a 51-atom quantum simulator, *Nature* **551**, 579 (2017).
 - [9] C. J. Turner, A. A. Michailidis, D. A. Abanin, M. Serbyn, and Z. Papić, Weak ergodicity breaking from quantum many-body scars, *Nat. Phys.* **14**, 745 (2018).
 - [10] M. Serbyn, D. A. Abanin, and Z. Papić, Quantum many-body scars and weak breaking of ergodicity, *Nat. Phys.* **17**, 675 (2021).
 - [11] P. Zhang, *et al.*, Many-body Hilbert space scarring on a superconducting processor, *Nat. Phys.* **19**, 120 (2023).
 - [12] G.-X. Su, H. Sun, A. Hudomal, J.-Y. Desaules, Z.-Y. Zhou, B. Yang, J. C. Halimeh, Z.-S. Yuan, Z. Papić, and J.-W. Pan, Observation of many-body scarring in a Bose-Hubbard quantum simulator, *Phys. Rev. Res.* **5**, 023010 (2023).
 - [13] P. Sala, T. Rakovszky, R. Verresen, M. Knap, and F. Pollmann, Ergodicity breaking arising from Hilbert space fragmentation in dipole-conserving Hamiltonians, *Phys. Rev. X* **10**, 011047 (2020).
 - [14] V. Khemani, M. Hermele, and R. Nandkishore, Localization from Hilbert space shattering: From theory to physical realizations, *Phys. Rev. B* **101**, 174204 (2020).
 - [15] L. Herviou, J. H. Bardarson, and N. Regnault, Many-body localization in a fragmented Hilbert space, *Phys. Rev. B* **103**, 134207 (2021).
 - [16] Z. C. Yang, F. Liu, A. V. Gorshkov, and T. Iadecola, Hilbert-space fragmentation from strict confinement, *Phys. Rev. Lett.* **124**, 207602 (2020).
 - [17] D. Hahn, P. A. McClarty, and D. J. Luitz, Information dynamics in a model with Hilbert space fragmentation, *SciPost Phys.* **11**, 074 (2021).
 - [18] S. Moudgalya, A. Prem, R. Nandkishore, N. Regnault, and B. A. Bernevig, in *Memorial Volume for Shoucheng Zhang* (World Scientific, Singapore, 2021), Chap. 7, pp. 147–209.
 - [19] S. Moudgalya and O. I. Motrunich, Hilbert space fragmentation and commutant algebras, *Phys. Rev. X* **12**, 011050 (2022).
 - [20] S. Moudgalya, B. A. Bernevig, and N. Regnault, Quantum many-body scars and Hilbert space fragmentation: A review of exact results, *Rep. Prog. Phys.* **85**, 086501 (2022).
 - [21] S. Pai, M. Pretko, and R. M. Nandkishore, Localization in fractonic random circuits, *Phys. Rev. X* **9**, 021003 (2019).
 - [22] M. Schulz, C. A. Hooley, R. Moessner, and F. Pollmann, Stark many-body localization, *Phys. Rev. Lett.* **122**, 040606 (2019).
 - [23] E. van Nieuwenburg, Y. Baum, and G. Refael, From Bloch oscillations to many-body localization in clean interacting systems, *Proc. Natl. Acad. Sci.* **116**, 9269 (2019).
 - [24] S. R. Taylor, M. Schulz, F. Pollmann, and R. Moessner, Experimental probes of Stark many-body localization, *Phys. Rev. B* **102**, 054206 (2020).
 - [25] R. Yao and J. Zakrzewski, Many-body localization of bosons in an optical lattice: Dynamics in disorder-free potentials, *Phys. Rev. B* **102**, 104203 (2020).
 - [26] Y.-Y. Wang, Z.-H. Sun, and H. Fan, Stark many-body localization transitions in superconducting circuits, *Phys. Rev. B* **104**, 205122 (2021).
 - [27] G. Zisling, D. M. Kennes, and Y. Bar Lev, Transport in Stark many-body localized systems, *Phys. Rev. B* **105**, L140201 (2022).
 - [28] E. Guardado-Sánchez, A. Morningstar, B. M. Spar, P. T. Brown, D. A. Huse, and W. S. Bakr, Subdiffusion and heat transport in a tilted two-dimensional Fermi-Hubbard system, *Phys. Rev. X* **10**, 11042 (2020).
 - [29] W. Morong, F. Liu, P. Becker, K. S. Collins, L. Feng, A. Kyprianidis, G. Pagano, T. You, A. V. Gorshkov, and C. Monroe, Observation of Stark many-body localization without disorder, *Nature* **599**, 393 (2021).
 - [30] Q. Guo, C. Cheng, H. Li, S. Xu, P. Zhang, Z. Wang, C. Song, W. Liu, W. Ren, H. Dong, R. Mondaini, and H. Wang, Stark many-body localization on a superconducting quantum processor, *Phys. Rev. Lett.* **127**, 240502 (2021).
 - [31] S. Scherg, T. Kohlert, P. Sala, F. Pollmann, B. Hebbe Madhusudhana, I. Bloch, and M. Aidelsburger, Observing non-ergodicity due to kinetic constraints in tilted Fermi-Hubbard chains, *Nat. Commun.* **12**, 4490 (2021).
 - [32] T. Kohlert, S. Scherg, P. Sala, F. Pollmann, B. Hebbe Madhusudhana, I. Bloch, and M. Aidelsburger, Exploring the

- regime of fragmentation in strongly tilted Fermi-Hubbard chains, *Phys. Rev. Lett.* **130**, 010201 (2023).
- [33] E. V. Doggen, I. V. Gornyi, and D. G. Polyakov, Stark many-body localization: Evidence for Hilbert-space shattering, *Phys. Rev. B* **103**, 100202 (2021).
- [34] R. Yao, T. Chanda, and J. Zakrzewski, Nonergodic dynamics in disorder-free potentials, *Ann. Phys.* **435**, 168540 (2021).
- [35] E. V. Doggen, I. V. Gornyi, and D. G. Polyakov, Many-body localization in a tilted potential in two dimensions, *Phys. Rev. B* **105**, 134204 (2022).
- [36] Q. Guo, C. Cheng, Z.-H. Sun, Z. Song, H. Li, Z. Wang, W. Ren, H. Dong, D. Zheng, Y.-R. Zhang, R. Mondaini, H. Fan, and H. Wang, Observation of energy-resolved many-body localization, *Nat. Phys.* **17**, 234 (2021).
- [37] D. J. Luitz, N. Laflorencie, and F. Alet, Many-body localization edge in the random-field Heisenberg chain, *Phys. Rev. B* **91**, 081103(R) (2015).
- [38] Y. Prasad and A. Garg, Initial state dependent dynamics across the many-body localization transition, *Phys. Rev. B* **105**, 214202 (2022).
- [39] D. J. Luitz, F. Alet, and N. Laflorencie, Universal behavior beyond multifractality in quantum many body systems, *Phys. Rev. Lett.* **112**, 057203 (2014).
- [40] N. Macé, F. Alet, and N. Laflorencie, Multifractal scalings across the many-body localization transition, *Phys. Rev. Lett.* **123**, 180601 (2019).
- [41] Q. Zhu, *et al.*, Observation of thermalization and information scrambling in a superconducting quantum processor, *Phys. Rev. Lett.* **128**, 160502 (2022).
- [42] Z.-C. Xiang, K. Huang, Y.-R. Zhang, T. Liu, Y.-H. Shi, C.-L. Deng, T. Liu, H. Li, G.-H. Liang, Z.-Y. Mei, H. Yu, G. Xue, Y. Tian, X. Song, Z.-B. Liu, K. Xu, D. Zheng, F. Nori, and H. Fan, Simulating Chern insulators on a superconducting quantum processor, *Nat. Commun.* **14**, 5433 (2023).
- [43] Y.-H. Shi, *et al.*, Probing spin hydrodynamics on a superconducting quantum simulator, *Nat. Commun.* **15**, 7573 (2024).
- [44] See Supplemental Material at <http://link.aps.org/supplemental/10.1103/PRXQuantum.6.010325>, which includes Ref. [60], for additional information about the experimental methods and a detailed discussion of the numerical simulations of the experiments.
- [45] S. P. Strong and A. J. Millis, Competition between singlet formation and magnetic ordering in one-dimensional spin systems, *Phys. Rev. Lett.* **69**, 2419 (1992).
- [46] M. Azzouz, L. Chen, and S. Moukouri, Calculation of the singlet-triplet gap of the antiferromagnetic Heisenberg model on a ladder, *Phys. Rev. B* **50**, 6233 (1994).
- [47] E. J. Torres-Herrera, J. Karp, M. Távora, and L. F. Santos, Realistic many-body quantum systems vs. full random matrices: Static and dynamical properties, *Entropy* **18**, 359 (2016).
- [48] M. Schreiber, S. S. Hodgman, P. Bordia, H. P. Lüschen, M. H. Fischer, R. Vosk, E. Altman, U. Schneider, and I. Bloch, Observation of many-body localization of interacting fermions in a quasirandom optical lattice, *Science* **349**, 842 (2015).
- [49] Y. Y. Atas, E. Bogomolny, O. Giraud, and G. Roux, Distribution of the ratio of consecutive level spacings in random matrix ensembles, *Phys. Rev. Lett.* **110**, 084101 (2013).
- [50] P. Roushan, *et al.*, Spectroscopic signatures of localization with interacting photons in superconducting qubits, *Science* **358**, 1175 (2017).
- [51] J. Hauschild, F. Heidrich-Meisner, and F. Pollmann, Domain-wall melting as a probe of many-body localization, *Phys. Rev. B* **94**, 161109(R) (2016).
- [52] D. Abanin, J. Bardarson, G. De Tomasi, S. Gopalakrishnan, V. Khemani, S. Parameswaran, F. Pollmann, A. Potter, M. Serbyn, and R. Vasseur, Distinguishing localization from chaos: Challenges in finite-size systems, *Ann. Phys.* **427**, 168415 (2021).
- [53] P. Sierant and J. Zakrzewski, Challenges to observation of many-body localization, *Phys. Rev. B* **105**, 224203 (2022).
- [54] H. Li, Y.-Y. Wang, Y.-H. Shi, K. Huang, X. Song, G.-H. Liang, Z.-Y. Mei, B. Zhou, H. Zhang, J.-C. Zhang, S. Chen, S. P. Zhao, Y. Tian, Z.-Y. Yang, Z. Xiang, K. Xu, D. Zheng, and H. Fan, Observation of critical phase transition in a generalized Aubry-André-Harper model with superconducting circuits, *npj Quantum Inf.* **9**, 40 (2023).
- [55] S. Boixo, S. V. Isakov, V. N. Smelyanskiy, R. Babbush, N. Ding, Z. Jiang, M. J. Bremner, J. M. Martinis, and H. Neven, Characterizing quantum supremacy in near-term devices, *Nat. Phys.* **14**, 595 (2018).
- [56] L. Zhang, Y. Ke, W. Liu, and C. Lee, Mobility edge of Stark many-body localization, *Phys. Rev. A* **103**, 023323 (2021).
- [57] X. Wei, X. Gao, and W. Zhu, Static and dynamical Stark many-body localization transition in a linear potential, *Phys. Rev. B* **106**, 134207 (2022).
- [58] V. D. Naik, F. Ballar Trigueros, and M. Heyl, Quantum hard disks on a lattice, *Phys. Rev. B* **110**, L220303 (2024).
- [59] M. Will, R. Moessner, and F. Pollmann, Realization of Hilbert space fragmentation and fracton dynamics in two dimensions, *Phys. Rev. Lett.* **133**, 196301 (2024).
- [60] Y. Yao, *et al.*, Observation of many-body Fock space dynamics in two dimensions, *Nat. Phys.* **19**, 1459 (2023).